ACS Sustainable Chemistry & Engineering

pubs.acs.org/journal/ascecg

Research Article

Integrated Portable Shrimp-Freshness Prediction Platform Based on Ice-Templated Metal–Organic Framework Colorimetric Combinatorics and Deep Convolutional Neural Networks

Peihua Ma, Zhi Zhang, Wenhao Xu, Zi Teng, Yaguang Luo, Cheng Gong, and Qin Wang*

Cite This: https://doi.org/10.1021/acssuschemeng.1c04704

Read Online

ACCESS | Metrics & More | Article Recommendations | Supporting Information

ABSTRACT: Real-time monitoring of food freshness is critical to reducing food waste and pursuing sustainable development. Cross-reactive artificial scent screening systems provide a promising solution for food freshness monitoring, but their commercialization is hindered by the low sensitivity or pattern-recognition inaccuracy. Leveraging the cutting-edge artificial intelligence and high-porosity nanomaterial, a cost-effective and versatile method was developed by incorporating metal–organic frameworks into smart food packaging via a colorimetric combinatorics sensor array. The whole UiO-66 family was screened by density functional theory calculations, and UiO-66-Br (due to the highest binding energy) was selected to construct sensor arrays on an ice-templated chitosan substrate (i.e., ice-templated dye@UiO-66-Br/Chitosan).

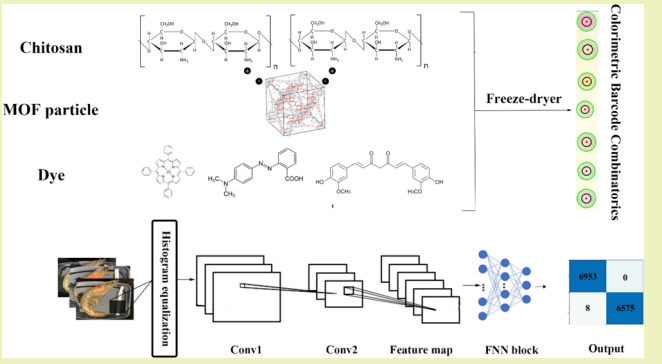

The physicochemical properties and morphologies of the fabricated sensor arrays were systematically characterized. The limit of detection of 37.17, 25.90, and 40.65 ppm for ammonia, methylamine, and trimethylamine, respectively, was achieved by the prepared composite film. Deep convolutional neural networks (DCNN), a deep learning algorithm family, were further applied to monitor shrimp freshness by recognizing the scent fingerprint. Four state-of-the-art DCNN models were trained using 31,584 labeled images and 13,537 images for testing. The highest accuracy achieved was up to 99.94% by the Wide-Slice Residual Network 50 (WISeR50). Our newly developed platform is integrated, sensitive, and non-destructive, enabling consumers to monitor shrimp freshness in real-time conveniently.

KEYWORDS: *metal–organic frameworks, sensor array, deep convolutional neural networks, shrimp freshness*

Downloaded via UNIV OF MARYLAND COLG PARK on December 15, 2021 at 18:55:46 (UTC).
See https://pubs.acs.org/sharingguidelines for options on how to legitimately share published articles.

INTRODUCTION

According to a recent report from the United States Department of Agriculture (USDA) in 2018, approximately 15% of perishable food is wasted at retail stores due to damage and spoilage, equaling $162 billion annually in the U.S.[1] Particularly, seafood has the highest percentage of waste compared to other food categories, with about 30% of the seafood products being wasted. Typically, more than half of the seafood waste or over 94 million pounds per year occurs at the end of the value chain, largely due to the conservative allocation of expiration dates on "sell by" tags.[1,2] In stark contrast to the arbitrary allocation of expiration dates, real-time measurements on individual products are predicted to effectively reduce the waste by 60%, which is worth $135 million per year in the U.S.[3]

As evidenced, there is a tremendous market value for developing real-time food freshness monitoring devices.[4] Recently, different approaches mimicking the mammalian olfactory system have been developed for the detection of explosives, drugs, and deleterious chemicals in foods.[5−7] One mainstream approach is artificial scent screening that requires two critical components: cross-reactive sensing and fingerprint pattern recognition.[8] Conventionally, cross-reactive sensing is achieved by integrating metal oxides[9] or colorimetric dyes onto sensor arrays.[10] While those sensors could target different molecules to generate a fingerprint pattern, they suffer from low adsorption rates and poor selectivity for volatile aroma compounds (VACs), resulting in poor accuracy and sensitivity.[4] In addition, the high complexity of the image-based pattern recognition cannot be efficiently analyzed by traditional statistical methods, e.g., discriminant analysis (LDA), principal component analysis (PCA), and hierarchical cluster analysis (HCA).[11]

Received: July 19, 2021
Revised: November 23, 2021

© XXXX American Chemical Society

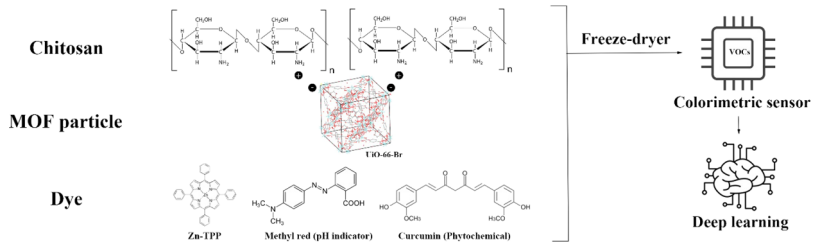

Figure 1. Fabrication of ice-templated colorimetric sensor array with the DCNN.

To address these challenges, we synergized artificial intelligence (AI), i.e., deep learning and porous framework nanomaterials in colorimetric sensor array systems. We adopted metal−organic frameworks (MOFs) to enhance sensitivity; due to the high-porosity structure with extremely high surface to bulk ratio, they have been widely applied in gas separation and storage, catalysis, biomolecule encapsulation, and battery.[12,13] Among different MOFs, we chose UiO-66 (named from the University of Oslo) for its high thermal, water, chemical, and mechanical stability, all of which arise from the high coordination number, strong bonds between inorganic blocks and the linker, and strong Zr−O bonds.[14] Furthermore, functional groups (such as $-NO_2$, $-NH_2$, $-OH$, $(COOH)_2$, $-(CH_3)_2$, and $-Br$) can be introduced into UiO-66 to increase the gas detection sensitivity and selectivity.[15] To address the long-standing challenge in accurate image recognition, we exploited the latest advances in AI and deep learning.[16] In particular, we employed the deep convolutional neural network (DCNN) and its derivative algorithms, which have found widespread success in the food field for dietary monitoring,[17] food quality detection,[18] food supply chain credit evaluation,[19] and predicting morbidity of gastrointestinal infections by food contamination.[20]

In this study, as shown in Figure 1, an ecofriendly sensor system was developed on ice-templated dye-loaded monoliths formed with chitosan, a low-cost biodegradable material, and UiO-66 (Dye@chitosan/UiO-66 hereafter). The system was designed and optimized with the help of the high-performance computer (HPC) by DFT and Grand Canonical Monte Carlo (GCMC) simulation. The adsorption ability of the sensor system was then evaluated for selective VACs. Finally, a fully supervised DCNN was trained using 31,584 labeled shrimp images with the sensor array. The overall objective of this study is to establish an MOF-based practical platform for real-time monitoring of seafood freshness based on advanced computer technology to effectively reduce food waste.

EXPERIMENTAL SECTION

Materials. Zirconium tetrachloride (99.5%), benzene-1,4-dicarboxylic acid (BDC, 98.0%), 2-2-bromoterephthalic acid (Br-BDC, 98.0%), *N*,*N*-dimethylformamide (DMF, 99.0%), Nile red, chitosan (medium molecular weight), ammonia hydrogen solution (25% in water), methylamine solution (33% in absolute ethanol), trimethylamine solution (45% in water), acetic acid (HAc, 99.9%), boric acid, (99.8%), 2-methoxyethanol (99%), and seven dyes were purchased from Sigma-Aldrich (St. Louis, MO, USA, details of dyes are presented in Table S1). All chemicals are in analytical grade. Jumbo tiger prawns (*Penaeus monodon*) at a mass of 14−16 g per shrimp were bought from Maine Ave Fish Market (Washington DC, USA). A microwave container (38 oz) was purchased from a local market (SafePro, MD, USA).

Computational Methods. Electronic structure calculations were performed using supercells to study the effect of confinement on molecular adsorption. The parent UiO-66 structure was taken from Jasuja and Walton,[21] and hydrogen(s) were replaced in the benzene ring with the functional groups of interest.[21] These calculations used a $1 \times 1 \times 1$ supercell with lattice parameters of ∼14−15 Å in each direction. The Vienna Ab Initio Simulation Package (VASP) was used at the PBE-D293 level with a 400 eV kinetic energy cutoff and one Γ-centered *k*-point. For structural optimization, the total energy and ionic force convergence criteria were 1×10^{-4} eV and 3×10^{-2} eV/Å, respectively. UiO-66 has a 3D cubic framework composed of $Zr_6O_4(OH)_4$ nodes linked with 1,4-benzenedicarboxylate linkers (BDC). It has centric octahedral cages (11 Å) connected to eight tetrahedral cages (8 Å) with triangular windows (6 Å).

Binding energies were defined in eq 1:

$$E_{\text{binding}} = E_{\text{adsorption complex}} - E_{\text{adsorbate}} - E_{\text{adsorbent}} \quad (1)$$

where E_{binding}, $E_{\text{adsorption complex}}$, $E_{\text{adsorbate}}$, and $E_{\text{adsorbent}}$ were the 1binding energy, total energy of the adsorption complex, total energy of the isolated adsorbate, and total energy of the isolated adsorbent, respectively.

GCMC simulations were used to calculate different isotherms at 200 K for UiO-66 and UiO-66-Br. At each pressure, the parameter of the equilibration step at 10,000,000 was set as a computer ensemble average. The framework atom was taken from the Universal Force Field (UFF). A charge of −0.482 was placed on the N nuclei and +0.964 at the center of mass. The Ewald and Group summation method was used for all interactions with atom-based van der Waals. All calculations mentioned above were based on a sorption isotherm module in Materials Studio (BIOVIA, v 5.51). The parameters mentioned above were taken from a previous study with some modifications.[22]

Preparation of UiO-66 and UiO-66-Br. UiO-66-Br was synthesized by a solvothermal method according to a previous report with minor modification.[23] First, $ZrCl_4$ (1.17 g, 5 mmol) and Br-BDC (1.23 g, 5 mmol) or benzene-1,4-dicarboxylic acid (0.83 g, 5 mmol) and acetic acid (1.0 mL) were dissolved in DMF (30 mL) at room temperature. Then, the mixture was placed in a Teflon-lined stainless-steel autoclave after adding 2 mL of deionized water and mixing completely. The autoclave was placed in an oil bath at 121 °C for 24 h. Afterward, the solution was cooled to room temperature for 30 min, and the resulting UiO-66 and UiO-66-Br particles were separated via centrifugation (12,096*g*, 10 min) at room temperature and washed three times with ethanol. The resulting white powder was dried in an oven at 40 °C for 4 h and tested by XRD and SEM for verification (Figure S1).

Ice-Templated Dye@Chitosan/UiO-66 Monoliths. In detail, 2.5 mL of chitosan solution (5 mg/mL, 2% HAc), 2.5 mL of UiO-66 / UiO-66-Br solution (5 mg/mL, 2% HAc), and 0.4 mL of dye solution (5 mg/mL in 2-methoxyethanol) were added in a bottle. The formulas for all dyes are presented in Table S1. After vigorous stirring, 0.2 mL of each solution was transferred to its assigned well on a 96-well plate, with a diameter of 6 mm for each pore. After carefully sealing the plate with a cap, the plate containing the solution was slowly immersed into a bath of liquid nitrogen for 5 min. The frozen sample was freeze-dried for approximately 48 h to form dry chitosan/UiO-66 monoliths. The monoliths of two types of UiO-66 particles were denoted as Chitosan/UiO-66 and Chitosan/UiO-66-Br. For the control, 2.5 wt % chitosan solution without UiO-66 or Uio-66-Br was

https://doi.org/10.1021/acssuschemeng.1c04704
ACS Sustainable Chem. Eng. XXXX, XXX, XXX−XXX

freeze-dried following the same procedure, and the acquired monolith was denoted as Chitosan. All monoliths with different dyes were adhered on a paper tape in the order of color in Table S1 to form the sensor array.

Calculation of Amine Gas Concentration. Detection experiments on amine gases were performed in standard Petri dishes (100 × 15 mm) with the temperature controlled at 20 °C. The colorimetric sensor array was passed on the cap of the Petri dishes. The required gas concentration was reached by injecting a certain volume of liquid analyte into the dish and sealed with Parafilm (i.e., ammonia (NH_3), methylamine (MA), and trimethylamine (TMA)). The resulting gas concentration (C_{ppm}) was calculated using the following equation (eq 2):

$$C_{ppm} = \frac{V_{\mu L} \times D_{mg/L} \times W}{M_{g/mol} \times V_L} \times 22.4 \times 10^7 \quad (2)$$

where $V_{\mu L}$ is the liquid analyte volume, $D_{mg/L}$ is the liquid density, W is the mass fraction of the liquid, $M_{g/mol}$ is the molecular weight of the liquid analyte, and V_L is the volume of Petri dishes.

MATERIAL CHARACTERIZATION

Fourier-Transform Infrared (FT-IR) Spectrometry. The samples (ice-templated UiO-66/chitosan and UiO-66-Br/Chitosan, 3−5 mg) were mounted onto a Jasco FT-IR 4100 spectrometer (Jasco Inc., Easton, MD, USA) coupled with an attenuated total reflectance (ATR) accessory. The infrared transmittance was acquired at the wavenumbers from 600 to 4000 cm^{-1} with a resolution of 2 cm^{-1}. Sixty-four repeated scans were undertaken for each sample. The spectra were averaged, smoothed, corrected for their baselines, and converted to absorbance with Spectra Manager software (Jasco Inc., Easton, MD, USA).[24]

Morphology Analysis. Samples were scooped into a 10 mm cup and placed into a shuttle, which was frozen conductively in a Styrofoam box, by placing the brass plates on the surface of a pre-cooled (−196 °C) brass bar whose lower half was submerged in liquid nitrogen. After 20−30 s, the shuttle containing the frozen sample was transferred to a Quorum PP2000 cryo-preparation chamber (Quorum Technologies, East Sussex, UK). The top layer of the frozen sample was cryo-fractured using a metal blade mounted inside the preparation chamber. All specimens were etched inside the cryo-preparation system to remove any surface contamination (condensed water vapor) by raising the temperature of the stage to −90 °C for 10−15 min. Following the etching, the temperature inside the chamber was lowered below −130 °C, and the specimens were coated with a 10 nm layer of platinum using a magnetron sputter head equipped with a platinum target inside the cryo-preparation chamber. The specimens were transferred to a pre-cooled (−130 °C) cryo stage in the scanning electron microscope (SEM) (Tescan XEIA FEG SEM, Brno, Czechia) for observation. An accelerating voltage of 5 kV was used to view the specimens. Images were captured using a 4pi Analysis System (Durham, NC).

Total Volatile Basic Nitrogen (TVB-N) Measurement. To mimic the storage conditions at supermarkets, 150 ± 10 g of fresh shrimps without any pretreatment was placed in a plastic box. One sensor array per package was attached to the inner side of the bag. Shrimps were stored at 4 °C before analysis.

To test the freshness of shrimps without the interference of image collection, a separate group of 24 (8 storage intervals × 3 parallel experiments) packages of shrimps was prepared for TVB-N testing. Ten grams of minced shrimp sample with shell was homogenized with 100 mL of distilled water (Ultra-Turrax T25, IKA, Staufen, Germany). The mixture was filtered for 30 min later to obtain a liquid sample. Then, 3 mL of boric acid absorbing solution (20 g/L) and 50 μL of pH indicator (methyl red:bromocresol green = 1:5, v/v) were added to the inner chamber of the Conway dish (diameter: 90 mm). In the outer chamber, 3 mL of potassium carbonate-saturated solution and 1 mL of sample liquid were added in sequence. The Conway dish was kept sealed and incubated at 37 °C for 2 h. The volatile amine gases were absorbed by boric acid as an absorbing solution. The abovementioned mixture was then titrated using 0.1 mol/L hydrochloric acid (HCl), and the amount of volatile amines was calculated with the following equation:

$$X = \frac{(v1 - v2) \times C \times 14}{m \times 0.05} \times 100 \quad (3)$$

where X is the TVB-N content in the sample (mg/100 g), $v1$ is the volume of 0.1 mol/L HCl used for the actual test (mL), $v2$ is the volume of 0.1 mol/L HCl used for the control test (mL), C is the HCl concentration (mol/L), 14 is the weight of nitrogen, and m is the weight of the sample (g).

MACHINE LEARNING

Circular Region of Interest (ROI) Identification. Hough circle transform was applied to recognize the color area of the sensor array. The circled candidates were produced by "voting" in the Hough parameter space and then selecting glocal maxima in an accumulator matrix. To obtain the best result, the inverse ratio of the resolution was set to 1, the upper threshold for the internal Canny edge detector was set to 10, the threshold for center detection was set to 9, and the range of radius to be detected was (20, 60) pixel. The ROI was extracted from the seven dye region labeled by the Hough circle transform.[25]

Database Preparation and Image Collection for DCNN Training. To collect data from the sensor, 10 s of a short video for each box was taken with shrimps at a certain storage interval. During the 10 s, the color and intensity of the background light in the photo box changed according to the program settings. Eight intervals that covered the spoilage process were selected. During the data collecting period, a portion of shrimp was examined for TVB-N, and others were used for image acquisition. Note that we changed the light that was included in the input images and photographed them with iPhone 11 Max Pro for training to fully mimic real testing scenarios. The 60 fps video was then randomly sampled at 30 fps and exported as an image set. Based on the actual measured TVB-N results and shrimp freshness criteria, we labeled samples with <30 mg N/100 g as fresh and >30 mg N/100 g as spoiled. Then, the final database was split into a training set and a testing set at the ratio 7:3. The final training set contained 31,584 labeled images, and the test set contained 13,537 images. The fresh-to-spoiled ratio was 1:1 in both training set and test set.

Network Architecture. With the acquired database, the DCNN was employed to train a food classification system. This system took images as input and classified them into two categories, i.e., Fresh and Spoiled. Four different DCNN architectures were compared for their effectiveness on classifying our novel food dataset: VGG,[26] ResNet-50,[27] Wide ResNet-50,[28] and Inception V3.[29] These four CNN

https://doi.org/10.1021/acssuschemeng.1c04704
ACS Sustainable Chem. Eng. XXXX, XXX, XXX−XXX

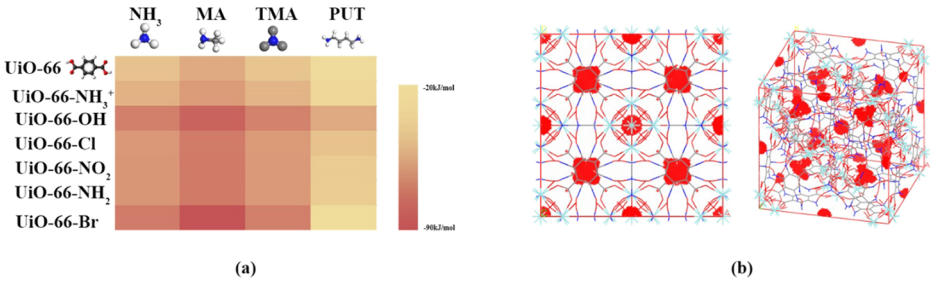

Figure 2. (a) Heat map of relative binding energy for four selected amine gases in functionalized UiO-66 materials determined from periodic PBE-D2 calculations. (b) Material Studio simulation indicates the COM probability distribution of the adsorbed NH_3 on the UiO-66-Br crystal.

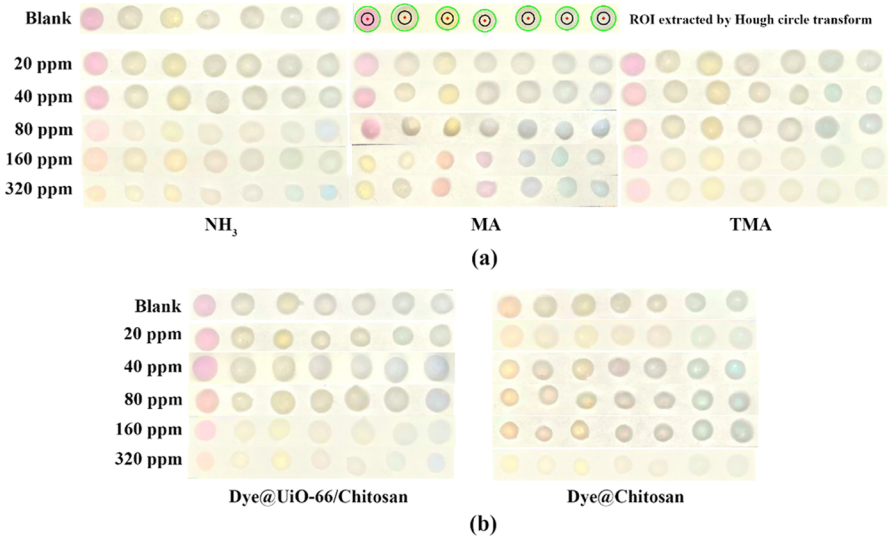

Figure 3. (a) Photographed images of color changes of Dye@UiO-66-Br/Chitosan sensor arrays exposed to NH_3, MA, and TMA as gas concentration increased from 20 to 320 ppm. (b) Photographed images of color changes of Dye@UiO-66/Chitosan and Dye@Chitosan sensor arrays exposed to NH_3.

architectures were pre-trained by the most commonly used and challenging image classification dataset. All experiments in this study were conducted on Windows Servers with Nvidia Quadro RTX 3000 GPUs. During the training and testing, the images were resized to 224 × 224 as inputs. The learning rate was set to 0.1 at the beginning of training and reduced to 0.05 and 0.01 when the test accuracy exceeded 70 and 80%, respectively. The momentum and weight decay were set to 0.9 and 0.0001, respectively.

RESULTS AND DISCUSSION

Identification of Materials for Selective Adsorption. During the storage, proteins in rotting shrimps are microbially decomposed into peptides and amino acids.[18] Over time, these components are further degraded into amines and ammonia, which will cause the color change of the sensor array.[4,5] Four amine gases (i.e., NH_3, MA, TMA, and putrescine (PUT)) typically generated during shrimp storage were simulated.

A previous research found that UiO-66-$(COOH)_2$ had a high CO_2 working capacity,[30] UiO-66-NH_2 was identified as the most promising material for vacuum swing adsorption,[31] and UiO-66-$(CH_3)_2$ diminished water adsorption by ∼50% compared with bare UiO-66.[21] However, due to the abundance of benzene ring modifications, the selection of appropriate functionalized materials for particular applications from overwhelming functional groups motivated the utilization of the computer method. Indeed, quantum chemistry calculations, especially density functional theory (DFT), were performed using clusters chosen to examine a wide range of functional groups for selective adsorption of ammonia.[32] Although methods to develop accurate force fields for molecular adsorption in MOFs from electronic structure calculations have developed rapidly in recent years, they still require extensive calculations for each specific adsorbent of interest. Here, we focus on using results from electronic structure calculations and identify the best choice of functional UiO-66 for selective VAC adsorption.

The binding energies for the aforementioned four amine gases were calculated for the [$-NH_3^+$, $-OH$, $-Cl$, $-NO_2$, $-NH_2$, $-Br$]-functionalized and unfunctionalized UiO-66 MOFs using DFT with PBE-D2 functions. Figure 2a compares the binding energy for four amine gases in functionalized UiO-66 materials. The PBE-D2 calculation is a useful quantification to consider situations with a low bulk phase concentration of adsorbing species.[15] Since our calculations have focused on individual binding sites for adsorbed molecules and the concentration of absorbed molecules was low in the food package, PBE-D2 was selected. It should be noted that this heuristic approach neglects possible synergistic effects between co-adsorbed species. The combination color close to red in the figure represents the strongest preferential binding energy. Among selected groups, $-Br$-functionalized UiO-66 MOFs showed the strongest preferential affinity for the three types of amine gases (i.e., NH_3, MA, and TMA), whereas unfunction-

https://doi.org/10.1021/acssuschemeng.1c04704
ACS Sustainable Chem. Eng. XXXX, XXX, XXX−XXX

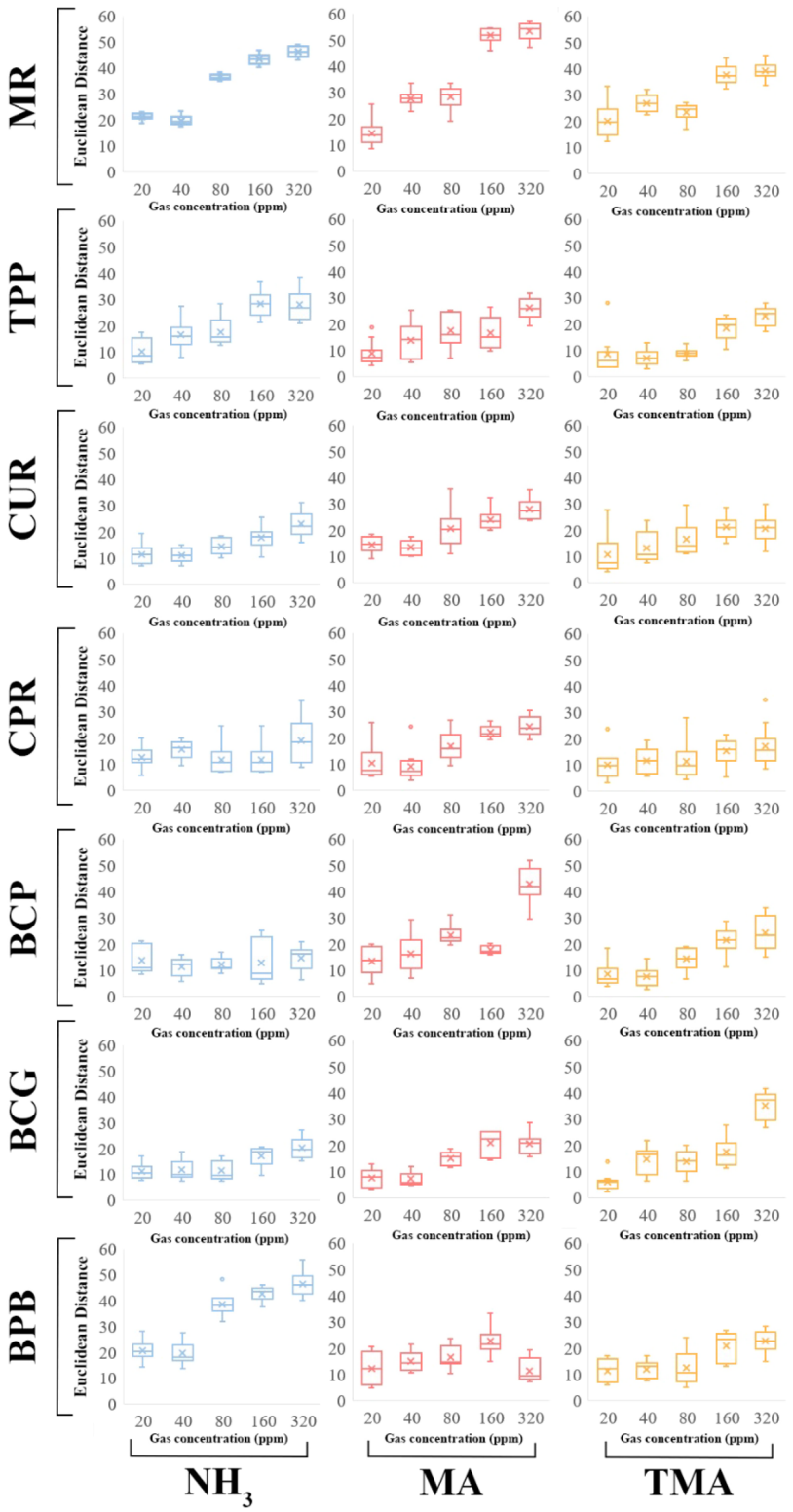

Figure 4. Boxplot of the ED distribution of different dyes based on UiO-66-Br/Chitosan for NH_3, MA, and TMA at different gas concentrations (from 20 to 320 ppm, n = 10).

alized UiO-66 showed the least. For example, UiO-66-Br binds MA (84.14 kJ/mol) more strongly than UiO-66-OH (77.42 kJ/mol) and the lowest bare UiO-66 (38.4 kJ/mol). Although calculated binding energies and experimental heat of adsorption are not precisely the same, they can be used to qualitatively screen and rank the binding affinity for the UiO-66 family.

Figure 2b illustrates the structure of UiO-66-Br with absorbed NH_3 molecules. The distribution of red dots represents the center of mass (COM), which indicates that amino gas molecules are more preferentially being adsorbed onto the BDC ligand sites than Lewis acid sites of Zr_6 nodes. According to the GCMC simulation result, the BDC ligand with the functionalized group was identified as the preferential

https://doi.org/10.1021/acssuschemeng.1c04704
ACS Sustainable Chem. Eng. XXXX, XXX, XXX−XXX

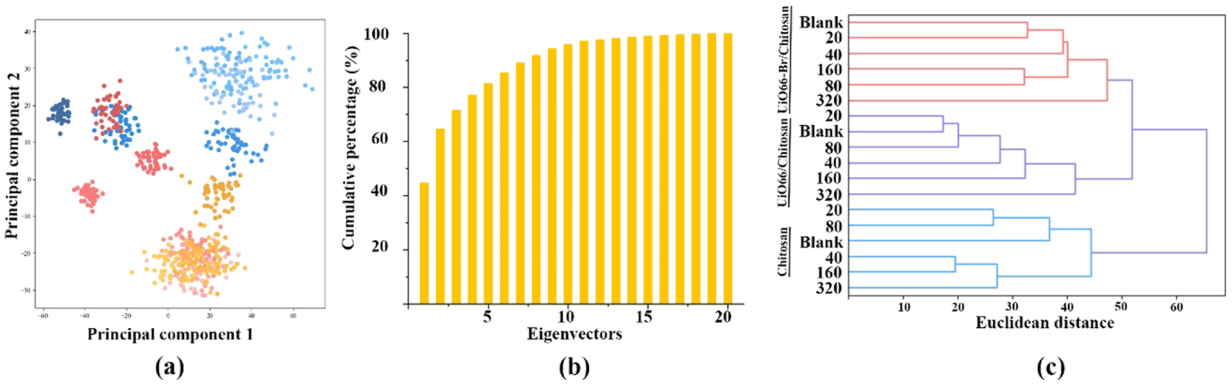

Figure 5. (a) Clusters of three sensor array systems: Dye@UiO-66-Br/Chitosan (red), Dye@UiO-66/Chitosan (blue), and Dye@chitosan (yellow) via a 2D PCA score plot. The color shade of the dot represents the concentration of ammonia gas concentration. The two dimensions plotted only encompass 44.73% of the total variance. (b) PCA score plot, the number of eigenvectors (i.e., principal components) needed to reach cumulative percentage (i.e., total variance). (c) Cluster tree produced by hierarchical cluster analysis showed that three colorimetric sensor array systems can be distinguished as being treated by different ammonia gas concentrations.

adsorption site for amino gas. In addition, the adsorption enthalpy $-\Delta H^{\circ}$ (i.e., isosteric heat) of water molecules on UiO-66-Br is calculated as 11.7 kJ/mol, which is much smaller than 84.14 kJ/mol for MA molecules and 67.4 kJ/mol for NH_3. From the thermodynamic aspect, amino gas molecules can replace pre-adsorbed water molecules on the UiO-66-Br material.[33] Hence, the moisture in the real atmosphere has a negligible impact on VAC sensing. Based on results of the above simulations, UiO-66-Br was selected as the candidate material for colorimetric sensor array preparation. In addition, to verify the simulation results, unfunctionalized UiO-66 was included as a control for the following experiments.

Sensor Array Validation on Response to VAC Standards. Because the sensor array was prepared on a paper base, it is cheap and can be integrated easily with existing package materials. To assess the ability of the colorimetric sensor array to be used as an indicator for VACs, the response of the Dye@UiO-66-Br/Chitosan sensor array to multiple gases, i.e., NH_3, MA, and TMA, was tested. The color changes of the array are dependent upon the concentration of selected gases, which provides a direct method for quantitative analysis.[6] Figure 3a shows the color changes of Dye@UiO-66-Br/Chitosan sensor arrays, which were treated with different concentrations of NH_3, MA, and TMA (photo by iPhone 11 Pro Max). All sensor arrays showed different color changes with these gases at concentrations ranging from 0 to 320 ppm. This is similar to mammalian olfactory receptors, where one scent molecule can bind to different receptors and one type of gas can trigger several sensors' color changes within the array. Meanwhile, the sensor array that responded to each gas formed a colorful fingerprint.

To describe the color distribution of the sensor, a color extraction and area recognition system based on the Hough circle transform was applied. The circled candidates are produced by "voting" in the Hough parameter space and then selecting glocal maxima in an accumulator matrix. The ROI was extracted from the seven dye region labeled by the Hough circle transform (see in Figure 3a). Then, 100 pixels were randomly generated from the ROI, and each variance of color components (red, green, and blue, RGB) of pixel was computed. According to previous reports, the variance is an important descriptor of the distribution of values, where lower values refer to a more even dye distribution and vice versa.[34] To achieve the quantitative analysis of color changes, the Euclidean distance (ED), an important value for the evaluation of color, was calculated by the RGB distance between selected concentrations and a blank.[7] As shown in Figure 4, ED values were overlapped under 40 ppm for seven dyes. As the gas concentration increased, some dyes such as MR showed increased ED, whereas others still showed insignificant changes (e.g., CPR, $n = 10$, $p < 0.05$). Meanwhile, ED values of the sensor array quantitatively followed the trends of the gas concentration. Corresponding to the previous report, higher concentrations of three types of amine gases (i.e., NH_3, MA, and TMA) displayed higher ED values but still some combinations did not show significant change (e.g., MA/BPB and NH_2/CPR).[5−7]

The limits of detection (LODs) of three amine gases are obtained at a signal-to-noise ratio of 3 following eqs 4 and 5:

$$S = \sum_{i=0}^{20} (|R_{\text{analyte}} - R_{\text{control}}| + |R_{\text{analyte}} - R_{\text{control}}| + |R_{\text{analyte}} - R_{\text{control}}|) \quad (4)$$

$$N = \sqrt{\frac{\sum_{i=0}^{20} ((R_{\text{control}} - \bar{R})^2 + (G_{\text{control}} - \bar{G})^2 + (B_{\text{control}} - \bar{B})^2)}{n - 1}} \quad (5)$$

where S is defined as the difference between the blank control (Control) and exposed groups (analyte) and n represents 10 independent experiments. The estimated LODs for NH_3, MA, and TMA were 37.17, 25.90, and 40.65 ppm, respectively. This result demonstrated that our sensor array had an adequate LOD (less than 35 ppm) for shrimp freshness detection in the food package. In addition, the ED values for each sensor before and after exposure to the same amount of gas were different. For example, after exposure to 320 ppm NH_3, MA, and TMA, the ED values for the MR sensor were 46.26, 53.13, and 39.13, respectively. This can be explained by the VASP simulation that the number of methyl groups in these three amine gases would impact the binding energy of the adsorption complex. Different chemical environments and the number of amino ($-NH_2$) groups in these selected amine gases would induce different color combinations in the sensor array. Meanwhile, this result was consistent with the observation from naked eyes. To further verify the computer simulation results, UiO-66/Chitosan and chitosan monolithic colorimetric sensor

https://doi.org/10.1021/acssuschemeng.1c04704
ACS Sustainable Chem. Eng. XXXX, XXX, XXX−XXX

Table 1. Comparison of Concentration and Equilibrium Time between Three Colorimetric Sensor Arrays

			standard deviation		
sensor array	range of concentration (ppm)	equilibrium time (s)	red	green	blue
UiO-66-Br/Chitosan	~80	420	0.09	0.04	0.10
UiO-66/Chitosan	~160	550	0.16	0.10	0.18
Chitosan	~320	720	0.18	0.13	0.22

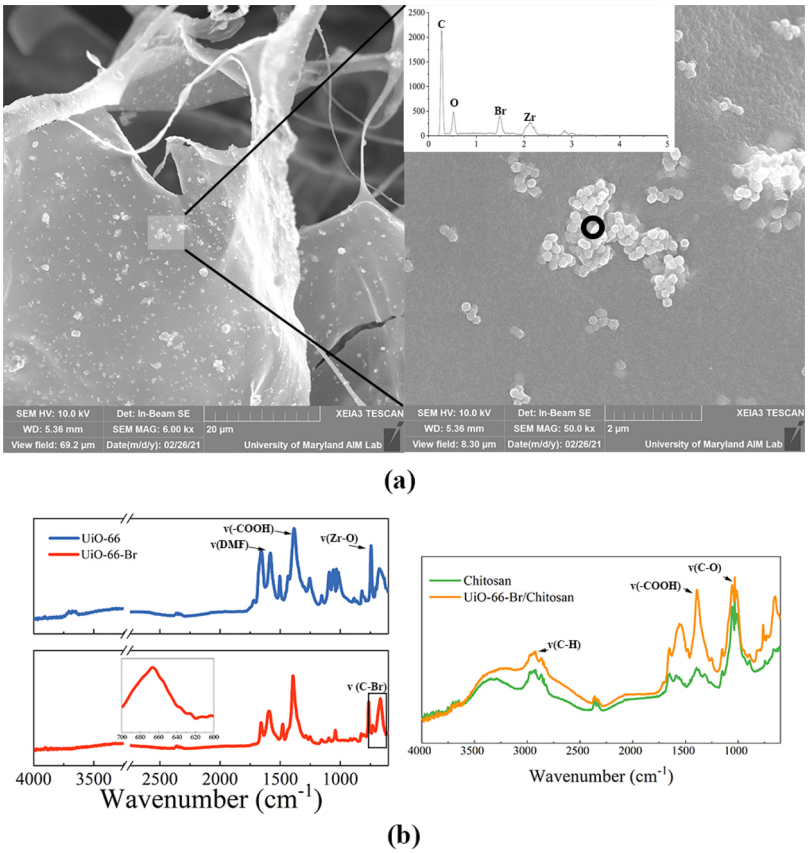

Figure 6. (a) SEM image of ice-templated methyl red@UiO-66-Br/Chitosan monolith with EDS result (left) and UiO-66-Br nanoparticles (right). (b) Infrared spectra of UiO-66 and UiO-66-Br nanoparticles (left). Infrared spectra of chitosan monoliths and UiO-66-Br/Chitosan monoliths (right).

arrays (i.e., Dye@UiO-66/Chitosan and Dye@Chitosan) were prepared for comparison. As shown in Figure 3b, two clear trends in color differences can be observed. First, all sensor arrays were affected by individual ammonia gas concentrations. Second, when observed by the naked eye, the colors of UiO-66-Br/Chitosan (see in Figure 3a, NH_3) and UiO-66/Chitosan were different from the Chitosan array. Meanwhile, adding UiO-66 or UiO-66-Br MOF particles led to the increasing turbidity of the system before freeze-drying in a preliminary research and also showed overall color change of the sensor array. Moreover, to all sensor arrays, the dyes spread uniformly and were distributed evenly. To quantitatively analyze the results, two traditional machine learning models (i.e., PCA and HCA) were used.

PCA is a widely used classification method.[35] Being evaluated by PCA, a 360 × 21 (20 duplicates × 6 gas concentration × 3 sensors arrays ×21 RGB values) dimensional matrix was acquired from the colorimetric sensor array. The PCA clustering result is shown in Figure 5a. PCA created several independent principal components (PCs) that maximally represent the whole matrix. According to the PCA score plot (Figure 5b), five PCs were needed to reach 80% of the total variance, and eight PCs were needed to reach 90% of the total variance. Here, due to the difficulties of drawing a high-dimensional plot, PCA clustering with two PCs (2D PCA score) was plotted, which represented 44.73% of the total variance. Two clear points can be concluded. First, the UiO-66-Br/Chitosan sensor array (red dots in Figure 5a) showed four cluster groups in the plot, and three high gas concentration groups were clearly distinguished between each other. For the UiO-66/Chitosan sensor array (blue dots), only two high gas concentration groups could be successfully separated, and only one group could be roughly classified for the chitosan sensor array (without UiO-66 particle, yellow dots). This could be explained by the VASP simulation results that different binding energies would induce different color combinations in the sensor array, which verified the hypothesis that the UiO-66-Br/Chitosan sensor array showed the best sensitivity. In addition, as the gas concentration increased, sensor arrays with different initial colors moved toward the same endpoint region (upper left area in Figure 5a). The possible reason was that the direction of dye

https://doi.org/10.1021/acssuschemeng.1c04704
ACS Sustainable Chem. Eng. XXXX, XXX, XXX−XXX

color change was the same in different sensors, so the color change endpoints were similar. Also, the PCA score showed that below 10 PCs, the variance increased with PCs and reached a platform after 15 PCs. This result could be explained by the over-adequate number of dye. For the ammonia gas response, the combination of multiple sensors improves the accuracy of the analysis, but there are some sensors in the array not involved. With HCA, Ward's minimum variance method was applied to determine gas-induced variations of the 21-dimensional RGB colorimetric sensor array (Figure 5c). The cluster tree showed that the three sensor arrays were clearly separated from each other. In addition, UiO-66-Br/Chitosan showed the highest ED value among different gas concentration groups. The results from PCA and HCA clustering intuitively revealed that the UiO-66-Br/Chitosan sensor array effectively discriminated NH_3 based on a cross-reactive colorimetric mechanism. Meanwhile, HCA results further confirmed that UiO-66-Br/Chitosan showed a better sensitivity when compared to the other two sensor arrays. Together, these results demonstrate that it is highly possible to use our colorimetric barcode to monitor shrimp freshness and other microbial metabolic processes in food storage.

Another comparison of the results between three types of colorimetric sensor arrays is shown in Table 1. To study the stability of sensor arrays, the variation in color shade was evaluated. At each concentration of NH_3, colorimetric sensor arrays were repeated 10 times and the color standard deviation after exposure to 40 ppm NH_3 was compared. A lower standard deviation indicates a more precise measurement and better stability. The result was consistent with the computer simulation analysis that the UiO-66-Br/Chitosan system showed the best accuracy when compared to bare UiO-66 and chitosan monoliths. In addition, the UiO-66-Br/Chitosan system showed the shortest equilibrium time, which could also be explained by the lower bonding energy simulated by VASP.

Characterization of Sensor Arrays. The UiO-66-Br/Chitosan system has fine fibers and sheet structure with voids (Figure 6a). SEM images revealed that MOF particles were trapped in the chitosan network after freeze-drying. The interspersed voids in the interwoven chitosan ribbons allow the impregnation of dye molecules. SEM of the MR-loaded sensor system revealed that UiO-66-Br penetrated through the voids during rehydration of padded dry sensor monoliths and got physically trapped in the fiber network. The morphology and size of UiO-66-Br particles were also determined using the SEM. The average diameter was in the range 132−163 nm, and most of the particles had clearly geometric boundaries. In addition, the EDS elemental analysis was carried out. The result confirmed that the particles trapped in the network were UiO-66-Br particles, which were composed mainly of carbon, oxygen, bromine, and zirconium, which was in accordance with the previously reported data.[23,36] The physicochemical characteristic of UiO-66-Br particles is shown showed in the Supporting Information (Table S2).

Figure 6b shows the infrared spectrum in the region of the skeletal mode of the samples. At lower frequencies, peaks due to O−H and C−H bending were mixed with the Zr−O peak (main bands at 746 cm^{-1}). In Zr−O_2 (Figure 6b, left), a twin peak at 725 and 620 cm^{-1} has been assigned to longitudinal and transverse peaks, respectively. Strong changes occurred between UiO-66 and UiO-66-Br due to the band associated with DMF (1667 cm^{-1}) and C−Br (668 cm^{-1}). The unique peaks of chitosan were observed at 3410 (ν_{O-H}), 1413 (δ_{N-H}), 1623 ($\nu_{C=O}$), and 1088 cm^{-1} (ν_{C-N}). After mixing UiO-66-Br with chitosan, the typical peaks of chitosan and MOF particles were all observed in the UiO-66-Br/Chitosan spectra, indicating that UiO-66-Br particles were successfully incorporated onto the chitosan via the adsorption process. In this study, UiO-66-Br was placed in chitosan dispersion until equilibrium was reached. According to a previous report, this mechanistic process often followed three consecutive steps: diffusion, attachment, and rearrangement/relaxation. Finally, the UiO-66-Br nanoparticle and chitosan chain formed a stable ice-templated macropores monolith system.[23,36]

Deep Learning-Enabled Freshness Recognition. For proof-of-concept purposes, we applied the newly developed sensor array to monitor the freshness of shrimp. To demonstrate the superiority of accuracy, the ED value method was applied and compared with deep learning models. Meanwhile, to obtain the best results, four state-of-the-art DCNN models were involved simultaneously, VGG, Inception V3, WISsR, and Resnet-50. The sensor arrays were glued to the bottom of lunch boxes without touching shrimp samples (Figure 7a).

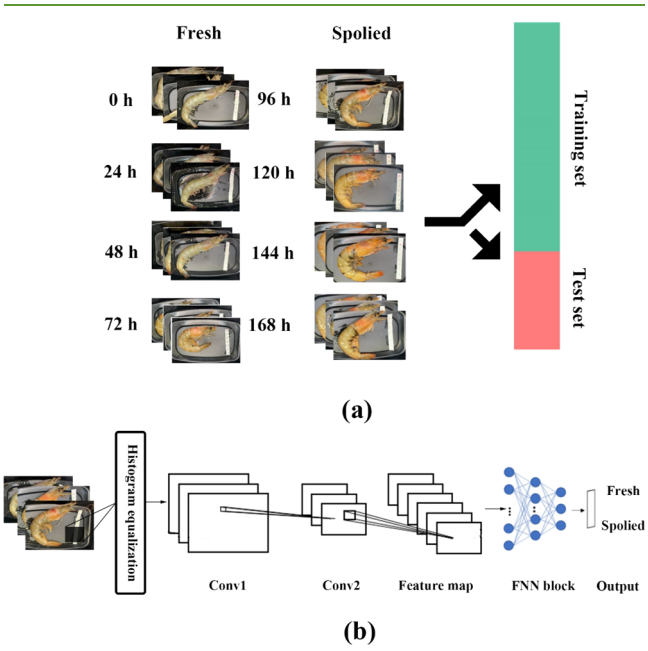

Figure 7. (a) Shrimp with a sensor array image database structure. The database contained 31,584 images for model training and 13,537 images for testing labeled with reference TVB-N results. (b) The DCNN models were used for shrimp freshness classification.

The shrimps were sealed in lunch boxes and stored at 4 °C. Images of the sensor arrays were taken at different time intervals by an iPhone 11 Max. According to a previous report, shrimps with TVB-N values less than 30 mg/100 g were considered fresh, whereas higher than 30 mg/100 g indicated being inedible and spoiled. To classify the sensor array into these two categories of freshness, the TVB-N value of the shrimp was tested by the Conway method. Then, images were labeled as fresh and spoiled according to this standard. The overall pattern changes in reference measurements of TVB-N contents during a period of 168 h cold storage period are illustrated in Figure S2.

A total of 45,121 images of shrimp and sensor array were obtained and formed a dataset for machine learning evaluation

https://doi.org/10.1021/acssuschemeng.1c04704
ACS Sustainable Chem. Eng. XXXX, XXX, XXX−XXX

of shrimp freshness. As mentioned in the Experimental Section, the dataset was first randomly split into a training subset and a testing subset with a ratio of 7:3, which means 31,584 images for model training and 13,537 images for testing. A true/false image classification network with different DCNN backbones, which comprised input, multiple convolutions, full connection, and output layers, was designed. The trained DCNN extracted features from images that contained sensor arrays and shrimp; afterwards, images were classified into one of the two categories, annotated fresh (true) and spoiled (false). Among four state-of-the-art DCNN models, the WISeR50 model showed the highest accuracy for freshness prediction, up to 99.94%, whereas VGG16 showed 98.51% (Table 2). In addition, to illustrate the superiority of deep learning, ED values were applied for comparison with the DCNN model. Following a previous research, we randomly selected 50 sensor array images from fresh and spoiled categories to assess the prediction accuracy of ED values.[6] In the end, the ED values achieved an overall prediction accuracy of 56.05%, which is significantly lower than those from DCNN models, indicating that it is difficult to distinguish fresh from spoiled using ED values in practice (Figure 8a).

Table 2. Accuracy Comparison Results between the ED Value Method and Four State-of-the-Art DCNN Models

models	accuracy
Euclidean distance	56.05%
VGG16	98.51%
ResNet50	99.75%
WISeR50	99.94%
Inception-V3	98.90%

Due to the superior accuracy of the DCNN algorithm, the model can reduce the interfering effect caused by photo-taking environments, including angle, lighting, and white balance, when compared to values from the ED method. This superiority of DCNN could be explained by the algorithm of the fitness model and data structure. RGB values of the sensor array do not linearly change with the concentration of gases, and thus the non-linear DCNN algorithm was consistent with mathematical similarity.[37] In addition, as epochs (i.e., the number of passes the algorithm completes through the entire database) increase, the loss (i.e., the difference between predicted and actual result) approaches 0 and remains in a plateau after 400 epochs (Figure 8b). This result proved that the training model was effective and after 400 epochs, all models achieved their highest accuracy for image-based freshness prediction. The comparison of four DCNN model confusion matrices is shown in Figure 8b whose diagonal showed the number of correctly classified samples, further illustrating the classification accuracy. In the statistical analysis of binary classification, the F_1 score is an indicator of test accuracy following eq 6:

$$F_1 = \frac{tp}{tp + 0.5(fp + fn)} \tag{6}$$

where tp is the number of true positives, fp is the number of false positives, and fn is the number of false negatives. It is the harmonic mean calculated from the precision and recall of the test, which might be a better measure to use when seeking a balance between precision and recall is needed. The F_1 score is often used in the field of information retrieval for measuring search, query classification, document classification, and machine learning. For this research, the WISeR50 DCNN model still showed the highest F_1 score, up to 0.9994, whereas the lowest is by VGG16, around 0.9853. This result confirmed that the WISeR50 DCNN model was preferable for identifying the freshness of shrimp with sensor array pictures.

Due to the higher accuracy of DCNN models than that of conventional machine learning models, it would be advantageous to apply it in colorimetric sensor array recognition and classification tasks. Furthermore, there are many other sensor arrays available for a good candidate, which could take advantage of the DCNN model and promising to achieve higher accuracy. This platform may be applied to other colorimetric sensor array systems or for a different task. The key advantage of this method is maintaining a high accuracy of image classification, while the image database can be established easily.

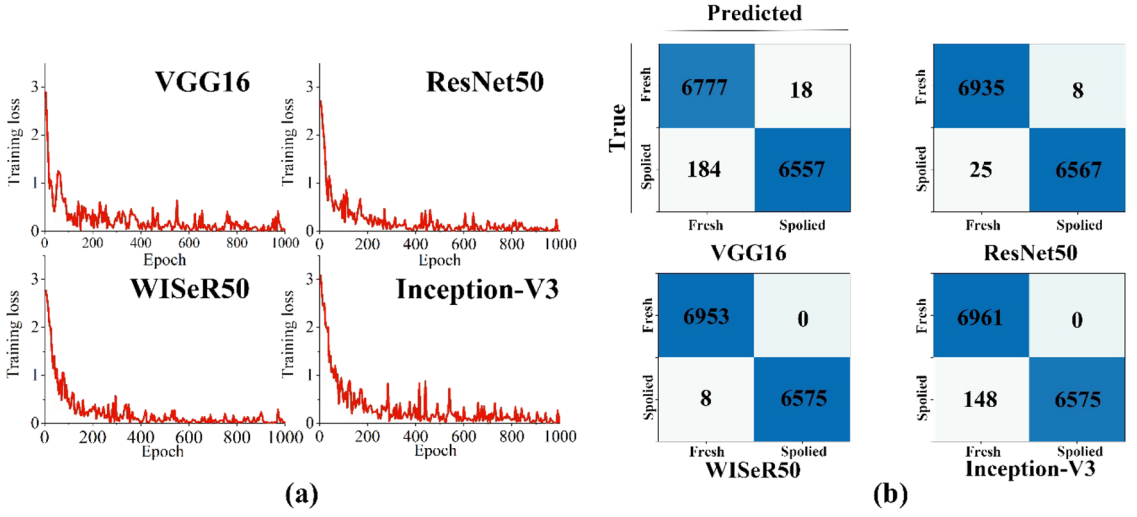

Figure 8. (a) Relation between DCNN model training loss with the increase in training epoch. (b) Confusion matrix of four DCNN models.

https://doi.org/10.1021/acssuschemeng.1c04704
ACS Sustainable Chem. Eng. XXXX, XXX, XXX−XXX

CONCLUSIONS

By leveraging an integrated cross-reactive colorimetric sensor array with a DCNN platform, a novel colorimetric sensor array was developed to rapidly and accurately monitor shrimp freshness in real time. The ice-templated Dye@chitosan/UiO-66-Br sensor system, which was optimized by DFT and GCMC simulation, showed significantly better sensitivity than unmodified UiO-66. The sensor array platform successfully detected gases released by spoiled shrimps (i.e., NH_3, MA, and TMA) and formed a scented fingerprint. All DCNN exhibited remarkably better accuracy than commonly used ED analysis, with the highest accuracy of 99.94% obtained from the WISeR50 model. Newly developed sensor array platform has great potential to be applied in smart food packages, and this work shed light on both reticular chemistry and artificial intelligence technology utilization in food research and industry.

ASSOCIATED CONTENT

Supporting Information

The Supporting Information is available free of charge at https://pubs.acs.org/doi/10.1021/acssuschemeng.1c04704.

(Table S1) List of biocompatible chromophore dyes on the colorimetric sensor array; (Table S2) comparison between UiO-66 and UiO-66-Br nanoparticles; (Figure S1) powder X-ray diffraction (PXRD) patterns of synthesized UiO-66 and UiO-66-Br compared with the simulated one for UiO-66, SEM images of UiO-66 nanoparticles, and SEM images of UiO-66-Br nanoparticles; and (Figure S2) pattern change of TVB-N content in *Penaeus monodon* during cold storage (PDF)

AUTHOR INFORMATION

Corresponding Author

Qin Wang − *Department of Nutrition and Food Science, College of Agriculture and Natural Resources, University of Maryland, College Park, Maryland 20742, United States;* orcid.org/0000-0002-7496-3921; Phone: 301-405-8421; Email: wangqin@umd.edu

Authors

Peihua Ma − *Department of Nutrition and Food Science, College of Agriculture and Natural Resources, University of Maryland, College Park, Maryland 20742, United States*

Zhi Zhang − *Department of Nutrition and Food Science, College of Agriculture and Natural Resources, University of Maryland, College Park, Maryland 20742, United States*

Wenhao Xu − *Department of Chemistry and Biochemistry, College of Computer, Mathematical and Natural Science, University of Maryland, College Park, Maryland 20742, United States*

Zi Teng − *Department of Nutrition and Food Science, College of Agriculture and Natural Resources, University of Maryland, College Park, Maryland 20742, United States; U.S. Department of Agriculture, Agricultural Research Service, Beltsville Agricultural Research Center, Food Quality Laboratory, Beltsville, Maryland 20705, United States;* orcid.org/0000-0002-6029-7024

Yaguang Luo − *U.S. Department of Agriculture, Agricultural Research Service, Beltsville Agricultural Research Center, Food Quality Laboratory, Beltsville, Maryland 20705, United States*

Cheng Gong − *Department of Electrical and Computer Engineering and Quantum Technology Center, University of Maryland, College Park, Maryland 20742, United States;* orcid.org/0000-0001-7714-6380

Complete contact information is available at: https://pubs.acs.org/10.1021/acssuschemeng.1c04704

Notes

The authors declare no competing financial interest.

ACKNOWLEDGMENTS

This work is partially supported by the USDA Hatch Fund and Maryland Agricutural Experimental Station (MAES). We appreciate generous help from Dr. Boce Zhang at the University of Massachusetts Lowell. The authors are grateful for the technical support of the Maryland NanoCenter at the University of Maryland. We thank the Chinese Scholarship Council for support P.M.'s learning and research.

REFERENCES

(1) Van der Werf, P.; Gilliland, J. A. In A systematic review of food losses and food waste generation in developed countries, *Proceedings of the Institution of Civil Engineers-Waste and Resource Management*, Thomas Telford Ltd: 2017; pp 66−77, DOI: 10.1680/jwarm.16.00026

(2) White, E. R.; Froehlich, H. E.; Gephart, J. A.; Cottrell, R. S.; Branch, T. A.; Baum, J. K., *Early effects of COVID-19 interventions on US fisheries and seafood*. 2020, DOI: 10.1111/faf.12525

(3) Corradini, M. G. Shelf life of food products: from open labeling to real-time measurements. *Annu. Rev. Food Sci. Technol.* **2018**, *9*, 251−269.

(4) Xiao-wei, H.; Xiao-bo, Z.; Ji-yong, S.; Zhi-hua, L.; Jie-wen, Z. Colorimetric sensor arrays based on chemo-responsive dyes for food odor visualization. *Trends Food Sci. Technol.* **2018**, *81*, 90−107.

(5) Yang, M.; Liu, X.; Luo, Y.; Pearlstein, A. J.; Wang, S.; Dillow, H.; Reed, K.; Jia, Z.; Sharma, A.; Zhou, B.; Pearlstein, D.; Yu, H.; Zhang, B. Machine learning-enabled non-destructive paper chromogenic array detection of multiplexed viable pathogens on food. *Nat. Food.* **2021**, *2*, 110−117.

(6) Guo, L.; Wang, T.; Wu, Z.; Wang, J.; Wang, M.; Cui, Z.; Ji, S.; Cai, J.; Xu, C.; Chen, X. Portable Food-Freshness Prediction Platform Based on Colorimetric Barcode Combinatorics and Deep Convolutional Neural Networks. *Adv. Mater.* **2020**, *32*, 2004805.

(7) Schroeder, V.; Evans, E. D.; Wu, Y.-C. M.; Voll, C.-C. A.; McDonald, B. R.; Savagatrup, S.; Swager, T. M. Chemiresistive sensor array and machine learning classification of food. *ACS sens.* **2019**, *4*, 2101−2108.

(8) Wang, T.; Wang, M.; Yang, L.; Li, Z.; Loh, X. J.; Chen, X. Cyber−Physiochemical Interfaces. *Adv.* **2020**, *32*, 1905522.

(9) Chen, J.; Chen, Z.; Boussaid, F.; Zhang, D.; Pan, X.; Zhao, H.; Bermak, A.; Tsui, C.-Y.; Wang, X.; Fan, Z. Ultra-low-power smart electronic nose system based on three-dimensional tin oxide nanotube arrays. *ACS Nano* **2018**, *12*, 6079−6088.

(10) Dai, J.; Ogbeide, O.; Macadam, N.; Sun, Q.; Yu, W.; Li, Y.; Su, B.-L.; Hasan, T.; Huang, X.; Huang, W. Printed gas sensors. *Chem. Soc. Rev.* **2020**, *49*, 1756−1789.

(11) Hu, W.; Wan, L.; Jian, Y.; Ren, C.; Jin, K.; Su, X.; Bai, X.; Haick, H.; Yao, M.; Wu, W. Electronic noses: from advanced materials to sensors aided with data processing. *Adv. Mater. Technol.* **2019**, *4*, 1800488.

(12) Anik, Ü.; Timur, S.; Dursun, Z. Metal organic frameworks in electrochemical and optical sensing platforms: a review. *Microchim. Acta* **2019**, *186*, 1−15.

(13) Ajdari, F. B.; Kowsari, E.; Shahrak, M. N.; Ehsani, A.; Kiaei, Z.; Torkzaban, H.; Ershadi, M.; Eshkalak, S. K.; Haddadi-Asl, V.; Chinnappan, A. A review on the field patents and recent

developments over the application of metal organic frameworks (MOFs) in supercapacitors. *Coord. Chem. Rev.* **2020**, *422*, 213441.
(14) Giannakoudakis, D. A.; Bandosz, T. J. Defectous UiO-66 MOF nanocomposites as reactive media of superior protection against toxic vapors. *ACS Appl. Mater. Interfaces* **2020**, *12*, 14678−14689.
(15) Demir, H.; Walton, K. S.; Sholl, D. S. Computational screening of functionalized UiO-66 materials for selective contaminant removal from air. *J. Phys. Chem. C* **2017**, *121*, 20396−20406.
(16) Ordovas, J. M.; Ferguson, L. R.; Tai, E. S.; Mathers, J. C. Personalised nutrition and health. *Bmj.* **2018**, *361*, bmj.k2173.
(17) Ege, T.; Yanai, K. Image-based food calorie estimation using recipe information. *IEICE Trans. Inf. Syst.* **2018**, *E101.D*, 1333−1341.
(18) Yu, X.; Wang, J.; Wen, S.; Yang, J.; Zhang, F. A deep learning based feature extraction method on hyperspectral images for nondestructive prediction of TVB-N content in Pacific white shrimp (Litopenaeus vannamei). *Biosyst. Eng.* **2019**, *178*, 244−255.
(19) Mao, D.; Wang, F.; Hao, Z.; Li, H. Credit evaluation system based on blockchain for multiple stakeholders in the food supply chain. *Int. J. Environ.* **2018**, *15*, 1627−1-21.
(20) Bisgin, H.; Bera, T.; Ding, H.; Semey, H. G.; Wu, L.; Liu, Z.; Barnes, A. E.; Langley, D. A.; Pava-Ripoll, M.; Vyas, H. J.; Tong, W.; Xu, J. Comparing SVM and ANN based machine learning methods for species identification of food contaminating beetles. *Sci. Rep.* **2018**, *8*, 1−12.
(21) Jasuja, H.; Walton, K. S. Experimental study of CO_2, CH_4, and water vapor adsorption on a dimethyl-functionalized UiO-66 framework. *J. Phys. Chem. C* **2013**, *117*, 7062−7068.
(22) Bernini, M.; Fairen-Jimenez, D.; Pasinetti, M.; Ramirez-Pastor, A.; Snurr, R. Screening of bio-compatible metal-organic frameworks as potential drug carriers using Monte Carlo simulations. *J. Mater. Chem. B* **2014**, *2*, 766−774.
(23) Ma, D.; Han, G.; Gao, Z. F.; Chen, S. B. Continuous UiO-66-Type Metal−Organic Framework Thin Film on Polymeric Support for Organic Solvent Nanofiltration. *ACS Appl. Mater. Interfaces* **2019**, *11*, 45290−45300.
(24) Mei, L.; Teng, Z.; Zhu, G.; Liu, Y.; Zhang, F.; Zhang, J.; Li, Y.; Guan, Y.; Luo, Y.; Chen, X.; Wang, Q. Silver Nanocluster-Embedded Zein Films as Antimicrobial Coating Materials for Food Packaging. *ACS Appl. Mater. Interfaces* **2017**, *9*, 35297−35304.
(25) Kuo, C.-J.; Wang, D.-C.; Chen, T.-T.; Chou, Y.-C.; Pai, M.-Y.; Horng, G.-J.; Hung, M.-H.; Lin, Y.-C.; Hsu, T.-H.; Chen, C.-C. In Improving Defect Inspection Quality of Deep-Learning Network in Dense Beans by Using Hough Circle Transform for Coffee Industry, *2019 IEEE Int. Conf. Syst. Man Cybern*. Man and Cybernetics (SMC), IEEE: 2019; pp. 798−805, DOI: 10.1109/SMC.2019.8914175
(26) Simonyan, K.; Zisserman, A., Very deep convolutional networks for large-scale image recognition. arXiv preprint arXiv:1409.1556 2014.
(27) He, K.; Zhang, X.; Ren, S.; Sun, J. *In Identity mappings in deep residual networks, European conference on computer vision*, Springer: 2016; pp 630−645, DOI: 10.1007/978-3-319-46493-0_38
(28) Zagoruyko, S.; Komodakis, N., Wide residual networks. arXiv preprint arXiv:1605.07146 2016.
(29) Szegedy, C.; Liu, W.; Jia, Y.; Sermanet, P.; Reed, S.; Anguelov, D.; Erhan, D.; Vanhoucke, V.; Rabinovich, A. In Going deeper with convolutions, *Proceedings of the IEEE conference on computer vision and pattern recognition*, 2015; pp 1−9, DOI: 10.1109/CVPR.2015.7298594
(30) Hu, Z.; Peng, Y.; Kang, Z.; Qian, Y.; Zhao, D. A modulated hydrothermal (MHT) approach for the facile synthesis of UiO-66-type MOFs. *Inorg. Chem.* **2015**, *54*, 4862−4868.
(31) Cmarik, G. E.; Kim, M.; Cohen, S. M.; Walton, K. S. Tuning the adsorption properties of UiO-66 via ligand functionalization. *Langmuir* **2012**, *28*, 15606−15613.
(32) Yu, D.; Ghosh, P.; Snurr, R. Q. Hierarchical modeling of ammonia adsorption in functionalized metal−organic frameworks. *Dalton Trans.* **2012**, *41*, 3962−3973.
(33) Kim, K. C.; Yu, D.; Snurr, R. Q. Computational screening of functional groups for ammonia capture in metal−organic frameworks. *Langmuir* **2013**, *29*, 1446−1456.
(34) Xiao-wei, H.; Zhi-hua, L.; Xiao-bo, Z.; Ji-yong, S.; Han-ping, M.; Jie-wen, Z.; Li-min, H.; Holmes, M. Detection of meat-borne trimethylamine based on nanoporous colorimetric sensor arrays. *Food Chem.* **2016**, *197*, 930−936.
(35) Granato, D.; Santos, J. S.; Escher, G. B.; Ferreira, B. L.; Maggio, R. M. Use of principal component analysis (PCA) and hierarchical cluster analysis (HCA) for multivariate association between bioactive compounds and functional properties in foods: A critical perspective. *Trends Food Sci. Technol.* **2018**, *72*, 83−90.
(36) Fu, Q.; Wen, L.; Zhang, L.; Chen, X.; Pun, D.; Ahmed, A.; Yang, Y.; Zhang, H. Preparation of ice-templated MOF−polymer composite monoliths and their application for wastewater treatment with high capacity and easy recycling. *ACS Appl. Mater. Interfaces* **2017**, *9*, 33979−33988.
(37) Ciocca, G.; Napoletano, P.; Schettini, R. CNN-based features for retrieval and classification of food images. *Computer Vision and Image Understanding* **2018**, *176-177*, 70−77.

https://doi.org/10.1021/acssuschemeng.1c04704
ACS Sustainable Chem. Eng. XXXX, XXX, XXX−XXX